Effect of cobalt alloying on the electrochemical performance of manganese oxide

nanoparticles nucleated on multiwalled carbon nanotubes

Effect of cobalt alloying on the electrochemical performance of manganese oxide nanoparticles nucleated on multiwalled carbon nanotubes

Sajad Yazdani[1,2]**, Raana Kashfi-Sadabad**[2]**, Alessandro Palmieri**[3]**, William E Mustain**[3] **and Michael Thompson Pettes**[1,2,4]

[1] Department of Mechanical Engineering, University of Connecticut, Storrs, CT 06269-3139, United States of America
[2] Institute of Materials Science, University of Connecticut, Storrs, CT 06269-3136, United States of America
[3] Department of Chemical & Biomolecular Engineering, University of Connecticut, Storrs, CT 06269-3222, United States of America

E-mail: michael.pettes@uconn.edu

CrossMark

Abstract

MnO is an electrically insulating material which limits its usefulness in lithium ion batteries. We demonstrate that the electrochemical performance of MnO can be greatly improved by using oxygen-functional groups created on the outer walls of multiwalled carbon nanotubes (MWCNTs) as nucleation sites for metal oxide nanoparticles. Based on the mass of the active material used in the preparation of electrodes, the composite conversion-reaction anode material $Mn_{1-x}Co_xO$/MWCNT with $x = 0.2$ exhibited the highest reversible specific capacity, 790 and 553 mAhg^{-1} at current densities of 40 and 1600 mAg^{-1}, respectively. This is 3.1 times higher than that of MnO/MWCNT at a charge rate of 1600 mAg^{-1}. Phase segregation in the $Mn_{1-x}Co_xO$ nanoparticles was not observed for $x \leqslant 0.15$. Capacity retention in $x = 0$, 0.2, and 1 electrodes showed that the corresponding specific capacities were stabilized at 478, 709 and 602 mAhg^{-1} respectively, after 55 cycles at a current density of 400 mAg^{-1}. As both MnO and CoO exhibit similar theoretical capacities and MnO/MWCNT and CoO/MWCNT anodes both exhibit lower performance than $Mn_{0.8}Co_{0.2}O$/MWCNT, the improved performance of the $Mn_{1-x}Co_xO$/MWCNT alloy likely arises from beneficial synergistic interactions in the bimetallic system.

Supplementary material for this article is available online

Keywords: lithium ion battery, conversion reaction anode, manganese oxide, cobalt oxide, carbon nanotubes

(Some figures may appear in colour only in the online journal)

Introduction

Manganese oxide based materials are attractive for lithium ion batteries due to their high abundance and low environmental impact [1]. Among different classes of these materials, MnO has a relatively high theoretical capacity of 755 mAhg^{-1} and low hysteresis voltage ($<$0.7 V). However, extremely high electrical resistivity and rapid capacity degradation are the limiting factors in reaching the theoretical capacity and achieving long service life [2–4]. Thus, it is highly desirable

---

[4] Author to whom any correspondence should be addressed.

Table 1. Summary of performance of state-of-the-art MnO-based materials. The theoretical capacities of MnO [3], CoO [25], and MWCNTs [2] are 755, 716, and 372 mAhg^{-1}, respectively.

Material	Number of cycles reported (#)	Current density used in stability test (mAg^{-1})	Final reversible capacity (mAhg^{-1})	High rate capacity (mAhg^{-1}) at current density (mAg^{-1})[a]	
Carbon-coated MnO [10]	2–150	50	650	213	(1600 mAg^{-1})
MnO/graphene nanosheets [20]	2–60	100	691[b]	390	(1000 mAg^{-1})
Nitrogen-doped MnO/graphene nanosheets [21]	2–90	100	772[b]	267	(1000 mAg^{-1})
MnO coated with N-doped carbon [22]	2–100	100	626[b]	314	(800 mAg^{-1})
MnO/reduced graphene oxide [26]	2–50	100	670[b]	331	(800 mAg^{-1})
MnO/C composites [27]	2–50	100	730	562	(1000 mAg^{-1})
MnO nanoparticle@mesoporous carbon composites [28]	2–80	100	784	609	(1000 mAg^{-1})
MnO coated with N-doped carbon [29]	2–400	200	640	451	(1000 mAg^{-1})
Hollow porous MnO/C microspheres [30]	2–50	100	700	260	(1000 mAg^{-1})
MnO/Carbon nanopeapods [31]	2–100	500	1047	551	(1500 mAg^{-1})
Porous MnO/N-doped carbon [32]	2–600	500	693	658	(1000 mA g^{-1})
MnO/MWCNT (present study)	2–55	400	478	177	(1600 mAg^{-1})
Mn$_{0.8}$Co$_{0.2}$O/MWCNT (present study)	5–55	400	709	642	(800 mAg^{-1})
				553	(1600 mAg^{-1})

[a] The reported higher current density rates up to 1600 mAg^{-1} were chosen as these are both more relevant to technological applications and can be more easily compared with the results of the current study;
[b] The reported specific capacity increased versus cycling most likely due to the formation of materials with higher oxidation states [33–35].

to improve the electrochemical performance of MnO-based materials by increasing their ultra-low electrical conductivity, on the order of 10^{-9} S cm^{-1} [5]. In pioneering reports, the electrochemical performance of MnO indicated a low-potential reaction with Li, although capacity was not promising [6]. Through microstructuring, an initial capacity of 650 mAhg^{-1} was obtained in inverse micelle-templated MnCO$_3$ [7]. However, this capacity degraded to 390 mAhg^{-1} after only 25 cycles. Capacity and stability were improved using a mixture of MnO and Mn$_3$O$_4$ nanoparticles confined to carbonized polyacrylonitrile (PAN) nanofibers with mesoporous features using electrospinning [8]. First cycle specific charge and discharge capacities of 1155 and 785 mAhg^{-1} were reported at a current rate of 50 mAg^{-1}, as well as a reversible capacity of 597 mAhg^{-1} after 50 cycles (23.6% decay with respect to the initial reversible capacity). Higher electrical conductivity of the carbon used in the preparation process and nanoscale electrochemically active materials were proposed to be responsible for the improved performance of their materials, as in other reports [9, 10]. A detailed review of MnO/carbon as well as MnO/reduced graphene oxide (rGO) composites is given in [2, 11]. As an alternative strategy to increasing conductivity, porous structures of pure MnO, MnO/CoO solid solutions and a nanocomposite of MnO and metallic cobalt (MnO/Co) were prepared by reduction of solutions of their corresponding carbonate precursors [12]. The MnO/Co structure exhibited improved reversible charge–discharge stability and it was concluded that deposition of the Co nanocrystals and the formation of a CoO surface layer were responsible for the enhanced performance. In addition, a significant number of previous reports on MnO-based materials show a dramatic increase in the capacity retention during

cycling [13–23] which is most likely due to the formation of phases with higher oxidation states and correspondingly higher theoretical capacities (such as Mn$_3$O$_4$ (936 mAhg^{-1}), Mn$_2$O$_3$ (1019 mAhg^{-1}) [11], MnO$_2$ (1230 mAhg^{-1}) [3]). However, in most cases even these materials exhibit poor high rate charge–discharge performance. Although the exact mechanism is still unclear, it has been reported that defect formations in MnO particles, arising from volume changes during cycling, can facilitate the oxidation [16, 24]. One feature common to previous investigations is that MnO, when used as an anode material, exhibits poor performance unless structural or chemical modifications are introduced. A summary is given in table 1. It should be noted that in most studies promising specific capacities are obtained only at very low current densities (50–100 mAg^{-1}) which greatly restricts their use in practical applications.

Here, we demonstrate a chemical route to nucleate Mn$_{1-x}$Co$_x$O nanoparticles on the outer walls of MWCNTs and obtain a capacity among the highest reported at application-relevant charge discharge rates. The structure-electrochemical performance relationship of Mn$_{1-x}$Co$_x$O composites with $x = 0$ and 0.2 grown directly on MWCNTs is found to strongly influence the electrochemical performance.

Methods

Chemicals

Manganese(II) acetate tetrahydrate Mn(CH$_3$COO)$_2 \cdot$ 4H$_2$O, cobalt(II) acetate tetrahydrate Co(CH$_3$COO)$_2 \cdot$ 4H$_2$O, ethyl alcohol (CH$_3$CH$_2$OH), multiwalled carbon nanotubes (MWCNTs

724769), potassium permanganate ($KMnO_4$), hydrogen peroxide (H_2O_2, 30%), and sodium nitrate ($NaNO_3$), sulfuric acid (H_2SO_4) 98% and ammonium hydroxide solution (NH_4OH) (with 28.0%–30.0% NH_3) basis were obtained from Sigma-Aldrich and used without further purification.

Synthesis of oxidized multiwalled carbon nanotubes

Oxidized multiwalled carbon nanotubes were prepared according to a procedure reported in [36], which is similar to the Hummer's method for preparation of graphene oxide [37]. In a typical synthesis, 1 g MWCNT was transferred into a round-bottom flask (250 ml) and 60 ml of concentrated sulfuric acid was added and stirred at room temperature for ~24 h. The flask was then heated in an oil bath, kept at 45 °C for 10 min, after which 0.1 g of sodium nitrate ($NaNO_3$) was added to the mixture. After 10 min while retaining the reaction temperature under 20 °C in an ice bath, 1 g of potassium permanganate ($KMnO_4$) was slowly added to the reaction. It should be noted that the addition of $KMnO_4$ should be slow and all the required safety precautions related to working with concentrated acids should be met. After 30 min, the solution was removed from the iced bath and after 5 min was transferred to an oil bath at 45 °C. After 30 min, 3 ml of deionized (DI) water was slowly added to the flask, and the reaction was proceeded by adding 5 and 40 ml of DI water after 5 and 10 min, respectively. After allowing the reaction to continue for another 15 min, the heat source was removed and 140 ml of DI water followed by 10 ml of 30% hydrogen peroxide (H_2O_2) solution were poured into the solution in order to stop the reaction. The mixture was then kept stirring at room temperature for 15 min. The obtained sample was washed with 5% HCl in DI water and centrifuged twice to remove any unreacted cations. The mixture was then continuously washed and centrifuged with DI water until a pH of ~5 was measured. Then the collected sample was dispersed in 100 ml of DI water and sonicated for 30 min. The final product was obtained by centrifugation and room temperature vacuum drying.

Synthesis of $Mn_{1-x}Co_xO$/MWCNT

Similar to [36, 38], 90 mg of the oxidized MWCNTs was ultrasonically dispersed in a 122.5 ml of 50:1 ethanol:DI water solution for 1 h. The mixture was transferred to a round-bottom flask (250 ml) to which 3 ml of $Mn(CH_3COO)_2 \cdot 4H_2O$ solution (0.6 M) in DI-water was added. A certain amount of Mn solution, x, was replaced by $Co(CH_3COO)_2 \cdot 4H_2O$ solution (0.6 M in DI water) for $x = 0.05, 0.10, 0.15$ and 0.20 samples. Afterwards, 2.5 ml of ammonium hydroxide was added to the mixture and the flask was transferred to an oil bath at 90 °C and re-fluxed for 24 h. The samples were collected by centrifugation at 7000 rpm and dried in vacuum at room temperature for 72 h. The dried samples were subsequently annealed in argon at 600 °C for 3 h with ramp 1 °C min^{-1} in order to crystalize the metal oxides and thermally reduce the partially oxidized MWCNTs.

Synthesis of $Mn_{1-x}Co_xO$ without MWCNTs

The samples without MWCNTs ($x = 0, 0.2$) were prepared by dissolving the stochiometric amounts of precursors in 122.5 ml of 50:1 ethanol:DI water solution. Similar to the synthesis described above, the mixture was transferred to a round-bottom flask (250 ml) and re-fluxed in an oil bath at 90 °C for 24 h. Specific to these samples without MWCNTs, the solution was poured in a Petri dish and placed in an oven at 60 °C in air until the solvent evaporated. The obtained powder was collected and annealed under argon at 600 °C for 3 h with ramp 1 °C min^{-1}.

Cell fabrication

Inks containing 70 wt% active materials, 20 wt% conductive carbon black (CNERGY Super C65, Imerys), and 10 wt% polyvinylidene fluoride (PVDF, Kynar blend) as the binder were prepared for fabrication of the half-cell 'cathode'. First, by repeated sonication and mechanical stirring of all ingredients overnight, a homogenous ink in N-methylpyrrolidone (NMP, Acros, 99.5% Extra Dry) was obtained. Copper foil (Alfa Aesar, 99.999%, thickness 0.002 in) as the current collector was roughened and cleaned by isopropanol. The prepared ink was sprayed onto copper foil to form a coating with a uniform thickness subsequently heated at 100 °C for 24 h under vacuum. The coated foil was pressed at 1500 lbs and weighed in order to obtain its mass loading. The active loadings were kept between 1.0 and 1.5 mg cm^{-2}. Coin cells were assembled in a half-cell configuration with lithium metal as the counter negative electrode (Alfa Aesar, 99.9%) and Celgard 2320 tri-layer PP/PE/PP as the separator in a 2.0 cm diameter coin cell (Hohsen Corp). Lithium hexafluorophosphate ($LiPF_6$, Acros 98%) (1 M) solution in ethylene carbonate (EC, Acros 99+%): dimethyl carbonate (DMC, Acros 98+%):diethyl carbonate (DEC, Acros 99%) with a ratio of (1:1:1) was used as the electrolyte on both sides of the separator (15 μl). The prepared cathode and counter negative electrode were cut into circles of 1.5 cm in diameter and were used with a 1.9 cm separator. All the battery components were pressed and sealed into the coin cell prior to removal from the glove box.

Electrochemical measurements

All the reported capacities were obtained based on the mass of the active materials. All electrochemical experiments were performed using an Arbin MSTAT battery test system.

Characterization

Powder x-ray diffraction (XRD) analyses were performed on a Bruker D2 Phaser with Cu K$_\alpha$ radiation ($\lambda = 1.54184$ Å) with an operating voltage and current of 30 kV and 10 mA. Transmission electron microscopy (TEM) analysis was conducted using a FEI Talos F200X TEM/STEM at an accelerating voltage of 200 kV, and chemical analyses were collected using STEM and energy dispersive x-ray spectroscopy (EDS) with HAADAF/BF detectors. Samples

were first dispersed in ethanol and then collected using copper grids covered with thin carbon films. X-ray photoelectron spectroscopy (XPS) was performed on a PHI model 590 spectrometer with multipoles (Φ Physical Electronics Industries Inc.), using Al K$_\alpha$ radiation ($\lambda = 1486.6$ eV). Electrochemical impedance spectroscopy (EIS) was conducted using an Autolab PGSTAT302 N Potentiostat (Eco Chemie) from 1000 kHz to 50 mHz with a 5 mV amplitude and a coin-cell open circuit voltage (2.2 V).

Results and discussion

The Mn$_{1-x}$Co$_x$O nanoparticles were grown on oxidized MWCNTs which were prepared by a modified Hummers method with a lower concentration of KMnO$_4$ [36, 37]. The mass ratio of Mn$_{1-x}$Co$_x$O to MWCNT was kept at 10:1. Mn(CH$_3$COO)$_2 \cdot$ 4H$_2$O and Co(CH$_3$COO)$_2 \cdot$ 4H$_2$O were used as the Mn and Co sources precursors. In order to reduce the hydrolysis rate and avoid formation or grouping of free particles, 0.5 ml of ammonium hydroxide solution was added to the mixture before heating. The samples were centrifuged and subsequently annealed in argon at 600 °C in order to crystalize the metal oxides and thermally reduce the partially oxidized MWCNTs [36]. In preparation of a working electrode, the Mn$_{1-x}$Co$_x$O/MWCNT materials were combined with carbon black and polyvinyldifluoride (PVDF) in a weight ratio of 70:20:10. Coin cells in half-cell configuration were used to perform the electrochemical measurements with lithium metal as the counter electrode. For a detailed explanation of the chemical synthesis and electrochemical measurements refer to the methods section.

X-ray powder diffraction measurements for the obtained products as shown in figure 1(a). At $x = 0$, all diffraction peaks can be indexed to a pure cubic crystal structure of MnO with the space group of $Fm\bar{3}m$ (225) according to JCPDS No. 01-077-2929. At $x = 1$, all peaks were assigned to CoO with the space group of $Fm\bar{3}m$ (225) according to JCPDS No. 48-1719. Cobalt substitution did not result in phase decomposition for $x \leqslant 0.15$. For $x \leqslant 0.15$ the results revealed small shifts in the peaks as shown in the inset of figure 1(a) implying slight changes in lattice d-spacing due to formation of a MnO-CoO solid solution obeying Vegard's law [39]. At $x = 0.2$, formation of a secondary phase is observed, where both the primary and secondary phases have d-spacings smaller than MnO and larger than CoO. This indicates the primary phase is closer in stoichiometry to MnO and the secondary phase is closer to CoO, but both phases are Mn$_{1-x}$Co$_x$O solid solutions. Raman spectroscopy indicated expected peaks for MWCNTs [40, 41], where D peaks at 1351.73 and 1350.31 cm^{-1} and G peaks at 1585.13 and 1583.75 cm^{-1} were observed for $x = 0$ and 0.2 samples, respectively (figure 1(b)). The D-to-G-peak intensity ratio was ~1.3 for both samples, indicating the high degree of disorder remaining in the MWCNTs arising from the surface oxidation process used in the synthesis of the composites. In addition, second order G' peaks at 2700 and 2701.62 and the $D + G$ peaks at 2935.05 and 2940.17 cm^{-1} were detected for

$x = 0$ and 0.2, respectively. The peaks located at 309.97, 358.39 and 650.20 cm^{-1} for $x = 0$ are characteristic of MnO [42, 43]. Peaks located at 297.95, 353.35 and 640.31 cm^{-1} for $x = 0.2$ are red shifted compared to those of the un-doped material, due to the alloying of CoO with the MnO host structure. The small peaks located at 172.04 and 461.42 cm^{-1} were assigned to CoO [44] in the $x = 0.2$ sample. High-resolution TEM analysis (figures 1(c), (d); and S1, supporting information is available at stacks.iop.org/NANO/28/155403/mmedia) confirms the nucleation and growth of MnO and Mn$_{0.8}$Co$_{0.2}$O nanoparticles onto the outer walls of the MWCNTs. Nanoparticle sizes were observed to be less than 100 nm for $x = 0$ and 0.2 (diameters ~7–85 nm, figure S2, supporting information).

The high-resolution XPS analysis of the C 1s peak for $x = 0$ and 0.2 samples at 284.7 eV (figure 2(a)), indicated the existence of C–C, C–O, C=O and COOH functional groups [45] at 284.6, 286.8, 287.3 and 299.93 eV respectively, with percentage area ratios of 10.21:3.93:1.55:1 for both samples. The oxygen bands at 529, 530.5, 531.8 eV were assigned to MnO, C–O and H–O bonds [46], respectively, as shown in figure 2(b). The band corresponding to absorbed water at ~533.5 eV was almost negligible (3.58 and 3.24% for $x = 0$ and 0.2, respectively). The Mn 2p$_{3/2}$ and Mn 2p$_{1/2}$ peaks at 640.5 and 652.1 eV, respectively, with peak-to-peak separation of 11.6 eV were well referenced to the Mn(II) oxidation state [33, 47] (figure 2(c)). Furthermore, Co–O species were detected in the XPS spectra of the $x = 0.2$ sample as shown in figure 2(d), and the XPS survey (figure S3, supporting information). The XPS spectra of Co 2p$_{3/2}$ and 2p$_{1/2}$ revealed characteristic peaks of CoO at 780 and 795.8 eV and their corresponding satellite peaks with binding energies of 785.3 and 801.8 eV are in agreement with the literature data [48–50]. It should be mentioned that the intense satellite peaks associated with high-spin Co(II) are due to multiple electron excitations, so-called shake-up [51, 52]. For $x = 0.2$, the Co XPS spectra show that the surface contains CoO, while the XRD results indicate the bulk of the material contains two phases of Mn$_{1-x}$Co$_x$O, the primary phase being Co poor and the secondary phase being Co rich, likely due to Co segregation towards the surface of the nanoparticles. Because of their rock salt structures and the comparable sizes of Mn^{2+} and Co^{2+} cations, MnO and CoO are known to be soluble over the entire Mn$_{1-x}$Co$_x$O ($0 \leqslant x \leqslant 1$) composition [53, 54] with a complete solubility at room temperature and a maximum of the miscibility gap in the calculated phase diagram occurring at a very low temperature (242 K) [55]. Despite the calculated complete solubility, phase separation and deviation from the solid solution composition can occur, especially at the surface as has been observed previously by XPS [53] and is observed in the present investigation.

In order to gain more information about the chemical composition of the Mn$_{1-x}$Co$_x$O/MWCNT, high resolution STEM-EDS analysis was performed as shown in figures 3(a)–(e), (see figures 3(f)–(j) for high resolution images) and figure S4, supporting information. The chemical maps showed spatially uniform dispersion of constituent elements throughout the nanoparticles. No detectable oxygen was
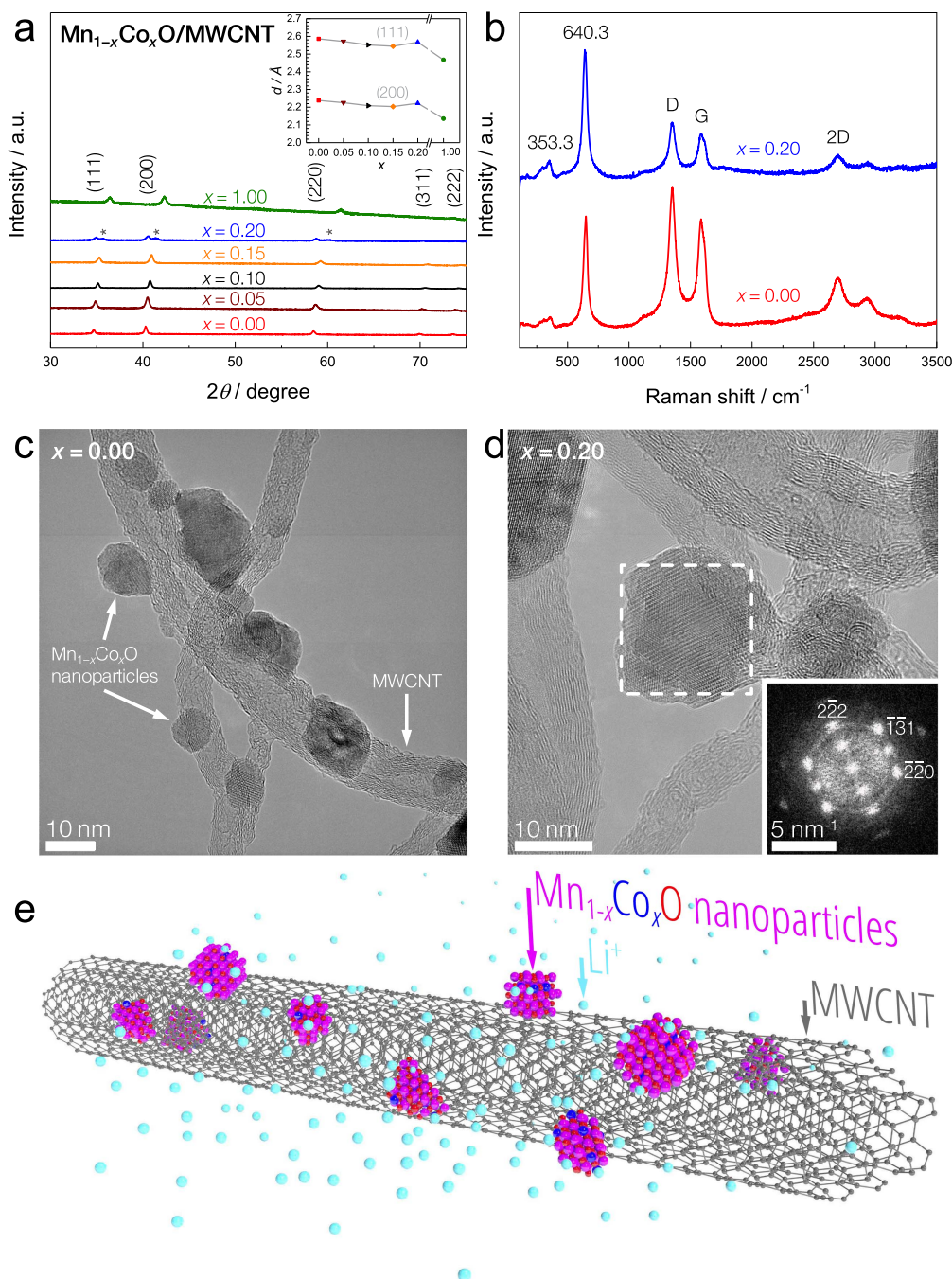
Figure 1. (a) XRD patterns for $Mn_{1-x}Co_xO$/MWCNT powders, the inset shows the lattice d-spacing variations versus the Co at% substitution, x. Phase segregation into primary Mn-rich and secondary Co-rich (asterisks) $Mn_{1-x}Co_xO$ phases is observed for $x = 0.2$. (b) Raman spectra for $Mn_{1-x}Co_xO$/MWCNT, $x = 0$ and 0.2. Transmission electron micrographs of (c) MnO and (d) $Mn_{0.8}Co_{0.2}O$ nanoparticles attached to MWCNTs. (d, inset) Fast fourier transform (FFT) pattern along the [$\bar{1}12$] zone axis. The lattice spacings of d_{111}, $d_{\bar{1}\bar{3}1}$, and $d_{\bar{2}\bar{2}0}$ were within 0.77, 0.12 and 0.39% of those obtained from the XRD data, respectively. (e) Schematic of the $Mn_{1-x}Co_xO$/MWCNT composite nanomaterial.

found on the MWCNTs (figures 3(b), (c)), although we note that Raman indicates a significant concentration of defects, and XPS indicates C–O, C=O and COOH functional groups.

The $Mn_{1-x}Co_xO$/MWCNT ($x = 0$, 0.2) nanocomposites were then used as the cathode material in a Li-ion half-cell as described in the methods section. The first cycle charge and discharge curves of the $x = 0.0$ and 0.2 samples are shown in figure 4(a) and were obtained at a current density of 40 mAg^{-1}. The samples showed initial charge capacities of 474 and

1044 mAhg^{-1} for $x = 0$ and 0.2, respectively at a current density of 40 mAg^{-1}. The features observed in the charge data were correlated with the reduction reaction of Mn^{2+} based on the reaction MnO + 2Li$^+$ + 2e^- → Mn + Li$_2$O, and the formation of the solid electrolyte interphase (SEI) [9]. The re-oxidation (Mn to Mn^{2+}) feature can be found in the slope of the discharge curves from 1 to 1.5 V versus Li/Li$^+$ (figure 4(a)). In addition, capacity fades of 25% and 23% from the first cycle to the second cycle were measured for $x = 0$ and
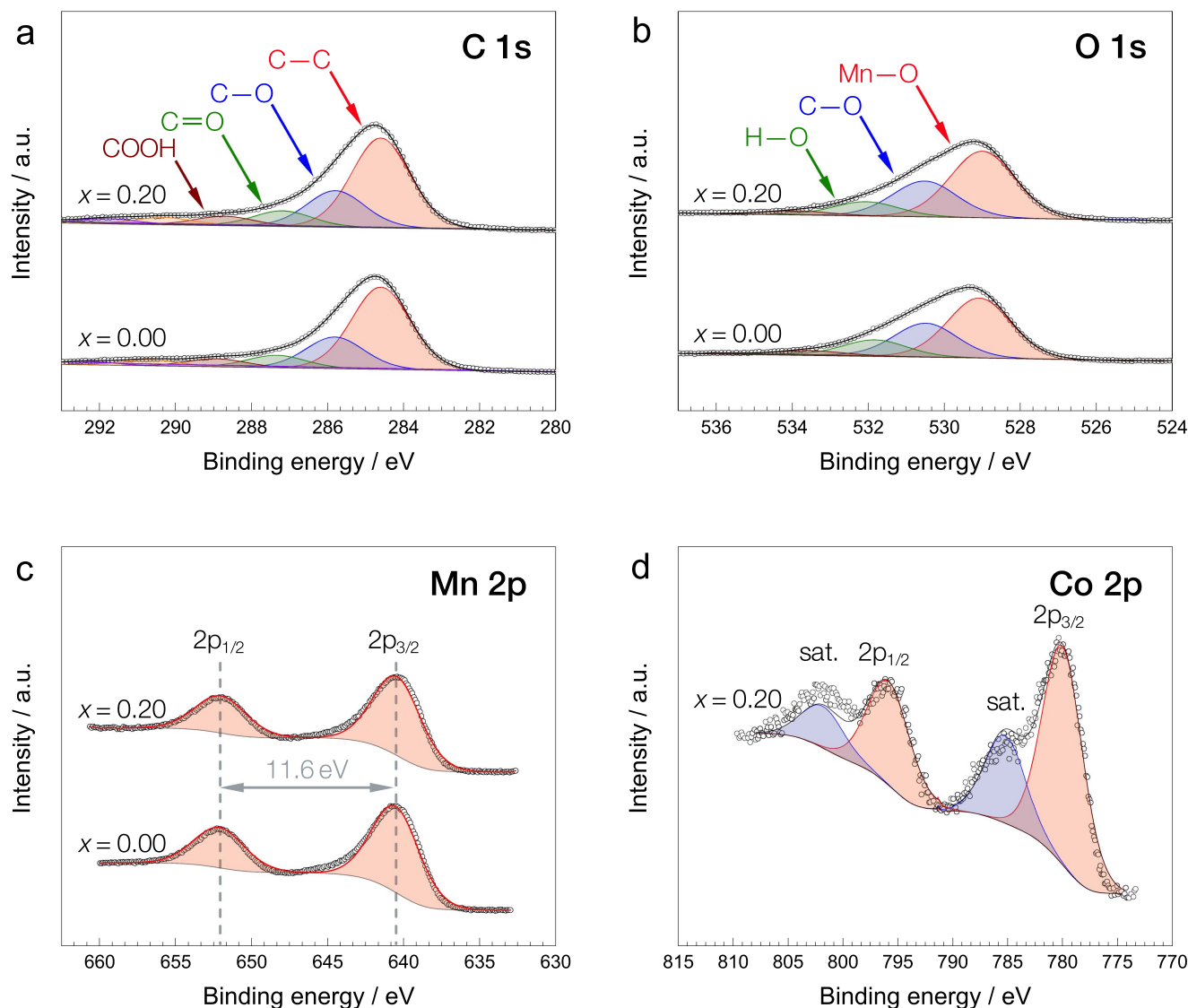
Figure 2. High resolution x-ray photoelectron spectroscopy (XPS) spectra of $Mn_{1-x}Co_xO$/MWCNT, $x = 0$ and 0.2, samples at a pass energy of 50 eV and sweep resolution of 0.1 eV for (a) C 1s, (b) O 1s, (c) Mn 2p and (d) Co 2p. Peaks centered at 785.3 and 801.8 eV denoted 'sat.' are assigned to the satellite peaks of Co(II) in CoO.

0.2 respectively (at a current density of 40 $mAhg^{-1}$), due to SEI formation.

Discussion

The charge–discharge behavior of the $x = 0.2$ sample at various current densities are demonstrated in figure 4(b). As expected, the achievable capacities decreased with increasing rates, though the results showed promising trends for high rate capacities. For example, 91% of the discharge capacity at a low current density of 40 mAg^{-1} was still achieved at a higher application-relevant rate of 400 mAg^{-1}. The rate performance of the nanocomposite materials is shown in figure 4(c). Both samples exhibited good high rate capacity performances. For instance, for $x = 0.2$, capacities of 790 and 642 $mAhg^{-1}$ were obtained at current densities of 40 and 800 mAg^{-1}, respectively. At the highest rate we tested, 1600 mAg^{-1}, the $x = 0.2$ sample exhibited a capacity of

553 $mAhg^{-1}$ which is still superior to the theoretical capacity of graphite (372 $mAhg^{-1}$) [2]. This value is higher than that of the reported state-of-the-art Mn-based materials with a higher degree of oxidation (therefore a higher theoretical capacity) at the same current density (390 $mAhg^{-1}$ for Mn_3O_4/reduced graphene oxide composites [56]). After cycling at 1600 mAg^{-1}, excellent reversibility was observed for $x = 0$, 0.2 samples, with measured capacities of 928 and 669 $mAhg^{-1}$ for $x = 0.2$ and 372 and 236 $mAhg^{-1}$ for $x = 0$ at current densities of 40 and 800 mAg^{-1}, respectively. The remarkable performance of the $x = 0.2$ composite at high rates is more striking when compared with the state-of-the-art literature data reported in table 1 (high capacity rate column). Figure 4(d) illustrates the capacity retention of both samples after 50 cycles from 0 to 3 V versus Li/Li^+ at a current density of 400 mAg^{-1}. After the first five formation cycles, specific capacities of 473 and 740 $mAhg^{-1}$ were maintained at 478 and 709 $mAhg^{-1}$ after 55 cycles at 400 mAg^{-1} for
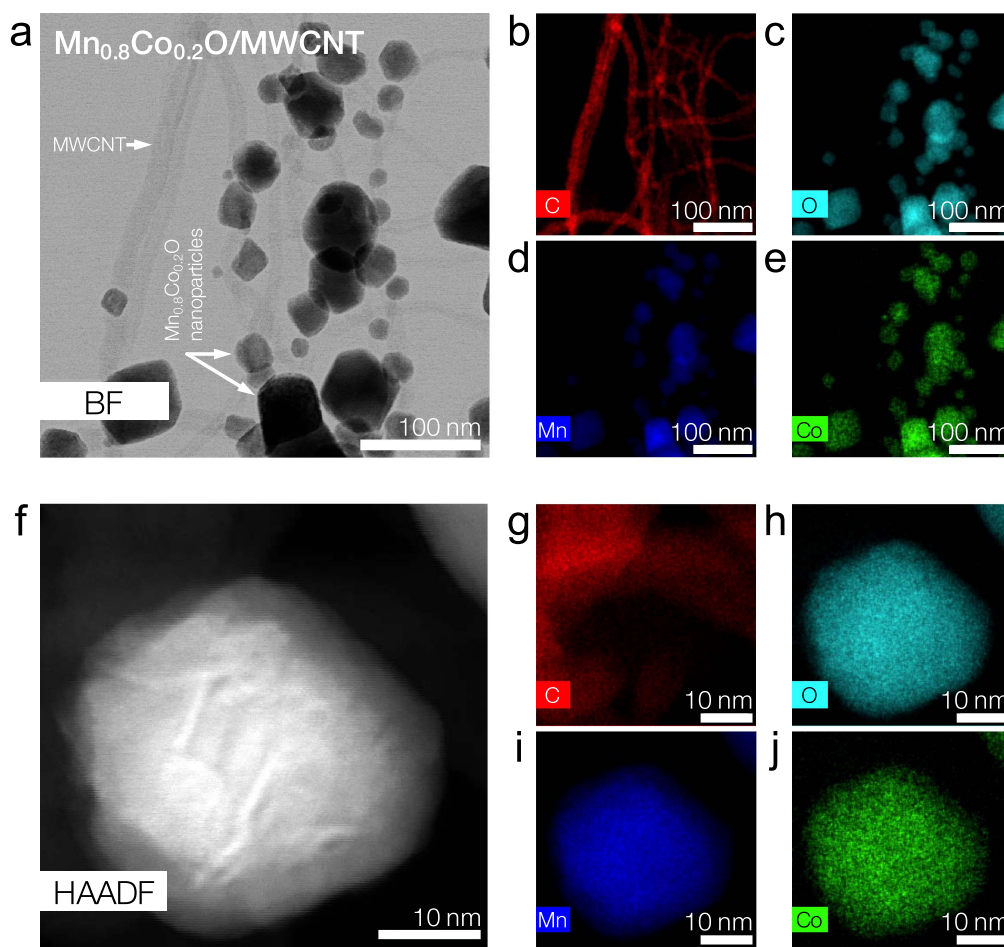
Figure 3. Scanning transmission electron microscopy-energy dispersive x-ray spectroscopy (STEM-EDS) analysis of the $Mn_{0.8}Co_{0.2}O/$ MWCNT composite. (a) Bright field (BF) STEM image and (b)–(e) corresponding STEM-EDS intensity maps of the (b) C, (c) O, (d) Mn, and (e) Co K-edge peaks. (f) High-resolution high-angle annular dark-field (HAADF) image and (g)–(j) corresponding STEM-EDS intensity maps of the (g) C, (h) O, (i) Mn, and (j) Co K-edge peaks.

$x = 0$ and 0.2, respectively. A comparison between $x = 0$, 0.5, 0.15, 0.2, 1 samples is given in the figure S5 in the supporting information. As can be seen, the cycling performances of $x = 0.15$ and 0.2 are close to each other indicating saturation of beneficial charge storage effects in the alloy. Both anodes ($x = 0.15$, 0.2) show higher capacity retentions than those of MnO/MWCNT and CoO/MWCNT, indicating the improved performance of alloys than their non-alloyed counterparts ($x = 0$, 1). For instance, the $x = 0.2$ anode exhibits a capacity 50% and 18% higher than those of $x = 0$ and 1 respectively, at the same current rate of $400 \, mAg^{-1}$ and after 55 cycles. This is despite the fact that the capacity of the CoO/MWCNT ($x = 1$) anode increases upon cycling which is attributed to formation of a material with a higher degree of oxidation and a higher theoretical capacity [2, 57]. The excellent stability of a similar preliminary nanocomposite was also demonstrated in a previous study [38].

In order to gain more insights into the role of MWCNTs in the observed high rate-capability of our materials, the electrical resistivities of MnO/MWCNT and pristine MnO were measured using a van der Pauw technique [58, 59] at room temperature. Pellets were fabricated from dried powders using a hydraulic press under 10 000 lb in a 12 mm diameter die. Electrical resistivities of 1.9×10^7 and $3.9 \times 10^{-1} \, \Omega \, cm$ were obtained from the averaged slopes of multiple current–voltage curves for MnO and MnO/MWCNT samples, respectively. The 8 orders of magnitude reduction in electrical resistivity of the MnO/MWCNT sample at a MWCNT loading of 40 wt% compared to our pure MnO indicated that nucleating electrochemically active nanomaterials onto MWCNTs is an effective strategy to boost electrical conductivity of conversion-reaction anode materials. The measured electrical resistivity of our pristine MnO is in close agreement with the bulk value ($1 \times 10^9 \, \Omega \, cm$) [5]. The improvement due to MWCNTs is further illustrated by comparison with the cycling performance of MnO and $Mn_{0.8}Co_{0.2}O$ without MWCNTs, where inferior capacities of 273 and $176 \, mAhg^{-1}$ are retained after 50 cycles at a current rate of $400 \, mAg^{-1}$ (figure S6, supporting information). Thus, the addition of MWCNTs increases the capacity retention at an application-relevant charge discharge rate of $400 \, mAg^{-1}$ by 1.75 and 2 times for $x = 0$ and 0.2 anodes, respectively. It should be noted that because the MWCNT weight ratio and oxidation degree play important roles in determining
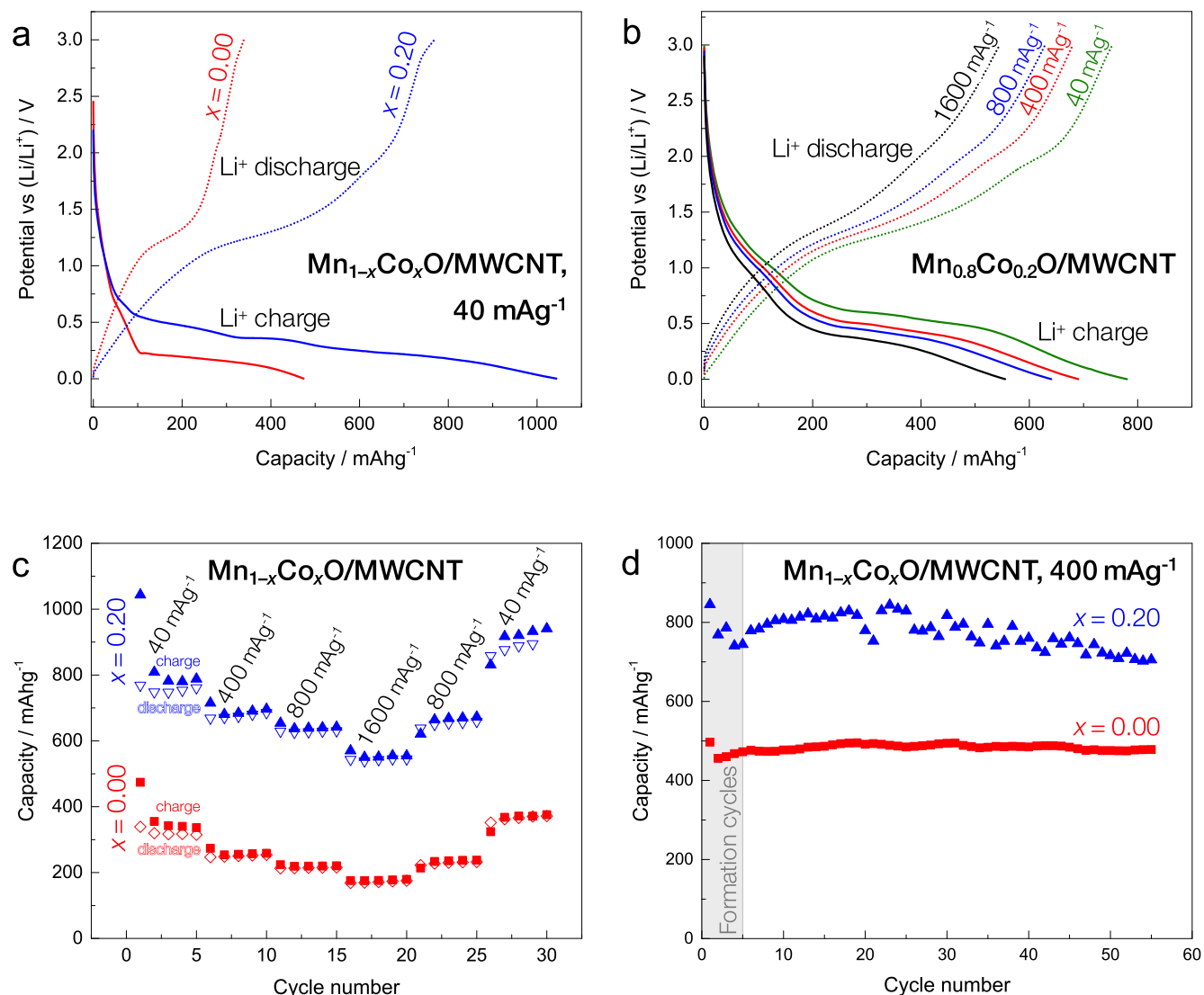
Figure 4. (a) First cycle charge–discharge profile of $Mn_{1-x}Co_xO$/MWCNT composites for $x = 0$ and 0.2. (b) Voltage versus specific capacity of $Mn_{0.8}Co_{0.2}O$/MWCNT at different charge–discharge current densities. (c) Current density dependence of the rate capability with cycling initiated at 40 mAg^{-1}. (d) Cycling performance for $x = 0$ and 0.2 initiated and maintained at 400 mAg^{-1} over a voltage range of 0–3 V. The first 5 cycles were considered as formation cycles.

the electrical conductivities of the samples, obtaining a correlation between these variables requires further study. In addition, the effectiveness of the Co substitution can be clearly observed by comparing the electrochemical performance of $x = 0$ and 0.2 samples as the specific capacity of the Co-alloyed sample is 3.1 times higher than that of the sample without Co at the highest measured current density of 1600 mAg^{-1}. This improved performance of the Co-containing samples likely arises due to possible synergistic interactions between Mn and Co in the structure because both MnO [3] and CoO [2] have similar theoretical capacities of 755 and 716 mAhg^{-1}, respectively. The mechanism responsible for improvement through Co-alloying can be better understood through EIS analysis. The EIS results reveal that Co-alloying facilitates the charge transfer in the composite electrode, as a smaller charge transfer resistance of 315 Ω was obtained for the sample with $x = 0.2$ compared to 700 Ω for $x = 0$ (figure S7 and table S1, supporting information). To the

best of our knowledge, there is no reported computational study describing the physical mechanism responsible for the experimentally-observed synergistic effect of Co-alloying on the electrical properties of MnO. However, several experimental studies [60–66] have reported improved electrochemical performances of other phases of manganese oxides by Co-alloying due to enhanced charged transport in the electrode and electrical conductivity of the material. The results of these studies including the present work stress the need for a comprehensive computational investigation in order to identify fundamental changes in the electronic properties of manganese oxides due to Co-incorporation.

Conclusion

In summary, $Mn_{1-x}Co_xO$ nanoparticles were synthesized directly on oxidized MWCNTs which were subsequently reduced thermally. Structural characterization suggested that

the Co incorporated into the MnO structure and no secondary phases were observed up to $x = 0.15$. The improvement in the specific capacity of the composite electrode at charge–discharge rates up to $1600 \, \text{mAg}^{-1}$ suggests that the method used here can be crucial in the modification of highly insulating earth-abundant materials such as MnO, making them promising candidates for battery applications [2, 67]. However, many additional investigations are still needed to clear the pathway for the (Mn,Co)O-based materials to reach their optimum potential in practical applications. For instance, the electrochemical contribution of each individual metal oxide and their interactions as an alloy are yet to be understood. The obtained results suggest future computational investigations are necessary to fully understand the role of Co-alloying in improving the charge transport. Identifying the effects of synthesis parameters such as the degree of oxidation of the MWCNTs, the active material to MWCNT weight ratio, and the annealing temperature can optimize the performance of the composite anode. Alloying with other transition metal oxides or alkali and alkaline earth metals will offer the possibility to further increase the electrochemical performance of MnO-based nanocomposite anode materials.

Acknowledgments

References

[1] Wei W, Cui X, Chen W and Ivey D G 2011 Manganese oxide-based materials as electrochemical supercapacitor electrodes *Chem. Soc. Rev.* **40** 1697

[2] Reddy M V, Subba Rao G V and Chowdari B V R 2013 Metal oxides and oxysalts as anode materials for Li ion batteries *Chem. Rev.* **113** 5364

[3] Roy P and Srivastava S K 2015 Nanostructured anode materials for lithium ion batteries *J. Mater. Chem.* A **3** 2454

[4] Nitta N and Yushin G 2014 High-capacity anode materials for lithium-ion batteries: choice of elements and structures for active particles *Part. Part. Syst. Charact.* **31** 317

[5] Bhide V G and Dani R H 1961 Electrical conductivity in oxides of manganese and related compounds *Physica* **27** 821

[6] Poizot P, Laruelle S, Grugeon S and Tarascon J-M 2002 Rationalization of the low-potential reactivity of 3d-metal-based inorganic compounds toward Li *J. Electrochem. Soc.* **149** A1212

[7] Aragón M J, Pérez-Vicente C and Tirado J L 2007 Submicronic particles of manganese carbonate prepared in reverse micelles: a new electrode material for lithium-ion batteries *Electrochem. Commun.* **9** 1744

[8] Ji L, Medford A J and Zhang X 2009 Porous carbon nanofibers loaded with manganese oxide particles: formation mechanism and electrochemical performance as energy-storage materials *J. Mater. Chem.* **19** 5593

[9] Liu J and Pan Q 2010 MnO/C nanocomposites as high capacity anode materials for Li-ion batteries *Electrochem. Solid-State Lett.* **13** A139

[10] Zhong K, Xia X, Zhang B, Li H, Wang Z and Chen L 2010 MnO powder as anode active materials for lithium ion batteries *J. Power Sources* **195** 3300

[11] Deng Y, Wan L, Xie Y, Qin X and Chen G 2014 Recent advances in Mn-based oxides as anode materials for lithium ion batteries *RSC Adv.* **4** 23914

[12] Kokubu T, Oaki Y, Hosono E, Zhou H and Imai H 2011 Biomimetic solid-solution precursors of metal carbonate for nanostructured metal oxides: MnO/Co and MnO-CoO nanostructures and their electrochemical properties *Adv. Funct. Mater.* **21** 3673

[13] Xiao Y and Cao M 2015 Carbon-anchored MnO nanosheets as an anode for high-rate and long-life lithium-ion batteries *ACS Appl. Mater. Interfaces* **7** 12840

[14] Liu D-H, Lu H-Y, Wu X-L, Hou B-H, Wan F, Bao S-D, Yan Q, Xie H-M and Wang R-S 2015 Constructing the optimal conductive network in MnO-based nanohybrids as high-rate and long-life anode materials for lithium-ion batteries *J. Mater. Chem.* A **3** 19738

[15] Wang J-G, Zhang C, Jin D, Xie K and Wei B 2015 Synthesis of ultralong MnO/C coaxial nanowires as freestanding anodes for high-performance lithium ion batteries *J. Mater. Chem.* A **3** 13699

[16] Luo W, Hu X, Sun Y and Huang Y 2013 Controlled synthesis of mesoporous MnO/C networks by microwave irradiation and their enhanced lithium-storage properties *ACS Appl. Mater. Interfaces* **5** 1997

[17] Xia P, Lin H B, Tu W Q, Chen X Q, Cai X, Zheng X W, Xu M Q and Li W S 2016 A novel fabrication for manganese monoxide/reduced graphene oxide nanocomposite as high performance anode of lithium ion battery *Electrochim. Acta* **198** 66

[18] Gu X, Yue J, Chen L, Liu S, Xu H, Yang J, Qian Y and Zhao X 2015 Coaxial MnO/N-doped carbon nanorods for advanced lithium-ion battery anodes *J. Mater. Chem.* A **3** 1037

[19] Zang J, Qian H, Wei Z, Cao Y, Zheng M and Dong Q 2014 Reduced graphene oxide supported MnO nanoparticles with excellent lithium storage performance *Electrochim. Acta* **118** 112

[20] Qiu D, Ma L, Zheng M, Lin Z, Zhao B, Wen Z, Hu Z, Pu L and Shi Y 2012 MnO nanoparticles anchored on graphene nanosheets via *in situ* carbothermal reduction as high-performance anode materials for lithium-ion batteries *Mater. Lett.* **84** 9

[21] Zhang K *et al* 2012 Synthesis of nitrogen-doped MnO/graphene nanosheets hybrid material for lithium ion batteries *ACS Appl. Mater. Interfaces* **4** 658

[22] Lu G, Qiu S, Lv H, Fu Y, Liu J, Li X and Bai Y-J 2014 Li-ion storage performance of MnO nanoparticles coated with nitrogen-doped carbon derived from different carbon sources *Electrochim. Acta* **146** 249

[23] Su K, Wang C, Nie H, Guan Y, Liu F and Chen J 2014 Facile template-free synthesis of 3D porous MnO/C microspheres with controllable pore size for high-performance lithium-ion battery anodes *J. Mater. Chem.* A **2** 10000

[24] Guo J, Liu Q, Wang C and Zachariah M R 2012 Interdispersed amorphous MnO$_x$–carbon nanocomposites with superior

electrochemical performance as lithium-storage material *Adv. Funct. Mater.* **22** 803

[25] Poizot P, Laruelle S, Grugeon S, Dupont L and Tarascon J M 2000 Nano-sized transition-metal oxides as negative-electrode materials for lithium-ion batteries *Nature* **407** 496

[26] Mai Y J, Zhang D, Qiao Y Q, Gu C D, Wang X L and Tu J P 2012 MnO/reduced graphene oxide sheet hybrid as an anode for Li-ion batteries with enhanced lithium storage performance *J. Power Sources* **216** 201

[27] Zhu W, Huang H, Zhang W, Tao X, Gan Y, Xia Y, Yang H and Guo X 2015 Synthesis of MnO/C composites derived from pollen template for advanced lithium-ion batteries *Electrochim. Acta* **152** 286

[28] Wang T, Peng Z, Wang Y, Tang J and Zheng G 2013 MnO nanoparticle@mesoporous carbon composites grown on conducting substrates featuring high-performance lithium-ion battery, supercapacitor and sensor *Sci. Rep.* **3** 2693

[29] Qiu T, Wang J, Lu Y and Yang W 2014 Facile fabrication of Chinese lantern-like MnO@N-C: a high-performance anode material for lithium-ion batteries *RSC Adv.* **4** 23027

[30] Xia Y *et al* 2013 Green and facile fabrication of hollow porous MnO/C microspheres from microalgaes for lithium-ion batteries *ACS Nano* **7** 7083

[31] Jiang H, Hu Y, Guo S, Yan C, Lee P S and Li C 2014 Rational design of MnO/carbon nanopeapods with internal void space for high-rate and long-life Li-Ion batteries *ACS Nano* **8** 6038

[32] Lu K, Xu J, Zhang J, Song B and Ma H 2016 General preparation of three-dimensional porous metal oxide foams coated with nitrogen-doped carbon for enhanced lithium storage *ACS Appl. Mater. Interfaces* **8** 17402

[33] Sun Y, Hu X, Luo W and Huang Y 2012 Porous carbon-modified MnO disks prepared by a microwave-polyol process and their superior lithium-ion storage properties *J. Mater. Chem.* **22** 19190

[34] Sun Y, Hu X, Luo W, Xia F and Huang Y 2013 Reconstruction of conformal nanoscale MnO on graphene as a high-capacity and long-life anode material for lithium ion batteries *Adv. Funct. Mater.* **23** 2436

[35] Tang X, Sui G, Cai Q, Zhong W and Yang X 2016 Novel MnO/carbon composite anode material with multi-modal pore structure for high performance lithium-ion batteries *J. Mater. Chem.* A **4** 2082

[36] Liang Y *et al* 2012 Oxygen reduction electrocatalyst based on strongly coupled cobalt oxide nanocrystals and carbon nanotubes *J. Am. Chem. Soc.* **134** 15849

[37] Hummers W S and Offeman R E 1958 Preparation of graphitic oxide *J. Am. Chem. Soc.* **80** 1339

[38] Palmieri A, Kashfi-Sadabad R, Yazdani S, Pettes M and Mustain W E 2016 High performance bi-metallic manganese cobalt oxide/carbon nanotube Li-ion battery anodes *Electrochim. Acta* **213** 620

[39] Vegard L 1921 Die konstitution der mischkristalle und die raumfüllung der atome *Z. Phys.* **5** 17

[40] Rao A M, Jorio A, Pimenta M A, Dantas M S S, Saito R, Dresselhaus G and Dresselhaus M S 2000 Polarized Raman study of aligned multiwalled carbon nanotubes *Phys. Rev. Lett.* **84** 1820

[41] Dresselhaus M S, Dresselhaus G, Saito R and Jorio A 2005 Raman spectroscopy of carbon nanotubes *Phys. Rep.* **409** 47

[42] Ramesh K, Chen L, Chen F, Liu Y, Wang Z and Han Y-F 2008 Re-investigating the CO oxidation mechanism over unsupported MnO, Mn_2O_3 and MnO_2 catalysts *Catal. Today* **131** 477

[43] Liao Q, Li N, Cui H and Wang C 2013 Vertically-aligned graphene@MnO nanosheets as binder-free high-performance electrochemical pseudocapacitor electrodes *J. Mater. Chem.* A **1** 13715

[44] He X, Song X, Qiao W, Li Z, Zhang X, Yan S, Zhong W and Du Y 2015 Phase- and size-dependent optical and magnetic properties of CoO nanoparticles *J. Phys. Chem.* C **119** 9550

[45] Li Y, Zhou W, Wang H, Xie L, Liang Y, Wei F, Idrobo J-C, Pennycook S J and Dai H 2012 An oxygen reduction electrocatalyst based on carbon nanotube-graphene complexes *Nat. Nanotechnol.* **7** 394

[46] Qiu S, Wang X, Lu G, Liu J and He C 2014 Facile synthesis of MnO and nitrogen-doped carbon nanocomposites as anode material for lithium ion battery *Mater. Lett.* **136** 289

[47] Moulder J, Stickle W, Sobol P and Bomben K 1992 *Handbook of X-ray Photoelectron Spectroscopy* (Eden Prairie, Minnesota: Perkin-Elmer Corporation) (https://phi.com/support/reference-material/handbook.html)

[48] Tan B J, Klabunde K J and Sherwood P M A 1991 XPS studies of solvated metal atom dispersed (SMAD) catalysts. Evidence for layered cobalt-manganese particles on alumina and silica *J. Am. Chem. Soc.* **113** 855

[49] Shen Z X *et al* 1990 Photoemission study of CoO *Phys. Rev.* B **42** 1817

[50] Langell M A, Anderson M D, Carson G A, Peng L and Smith S 1999 Valence-band electronic structure of Co_3O_4 epitaxy on CoO(100) *Phys. Rev.* B **59** 4791

[51] McIntyre N S and Cook M G 1975 X-ray photoelectron studies on some oxides and hydroxides of cobalt, nickel, and copper *Anal. Chem.* **47** 2208

[52] Frost D C, McDowell C A and Woolsey I S 1972 Evidence for multiplet splitting of 2p photoelectron lines of transition metal complexes *Chem. Phys. Lett.* **17** 320

[53] Langell M A, Gevrey F and Nydegger M W 2000 Surface composition of $Mn_xCo_{1-x}O$ solid solutions by x-ray photoelectron and Auger spectroscopies *Appl. Surf. Sci.* **153** 114

[54] Wang F, Zhang S, Bai D, Zhang F and Xu S 2016 Graphene-supported binary active $Mn_{0.25}Co_{0.75}O$ solid solution derived from a CoMn-layered double hydroxide precursor for highly improved lithium storage *RSC Adv.* **6** 19716

[55] Bergman B and Ågren J 1986 Thermodynamic assessment of the system CoO-MnO *J. Am. Ceram. Soc.* **69** 877

[56] Wang H, Cui L-F, Yang Y, Sanchez Casalongue H, Robinson J T, Liang Y, Cui Y and Dai H 2010 Mn_3O_4−graphene hybrid as a high-capacity anode material for lithium ion batteries *J. Am. Chem. Soc.* **132** 13978

[57] Yu Y, Chen C-H, Shui J-L and Xie S 2005 Nickel-foam-supported reticular CoO–Li_2O composite anode materials for lithium ion batteries *Angew. Chem. Int. Ed.* **44** 7085

[58] Van der Pauw L J 1958 A method of measuring the resistivity and Hall coefficient on lamellae of arbitrary shape *Philips Tech. Rev.* **20** 220

[59] Thurber W R 2010 Resistivity and Hall Measurements, National Institute of Standards and Technology (https://nist.gov/pml/engineering-physics-division/resistivity-and-hall-measurements)

[60] Sharma P K, Moore G J, Zhang F, Zavalij P and Whittingham M S 1999 Electrical properties of the layered manganese dioxides $M_xMn_{1-y}Co_yO_2$, M = Na, K *Electrochem. Solid-State Lett.* **2** 494

[61] Kim J H, Park C W and Sun Y K 2003 Synthesis and electrochemical behavior of $Li[Li_{0.1}Ni_{0.35-x/2}Co_xMn_{0.55-x/2}]O_2$ cathode materials *Solid State Ion.* **164** 43

[62] Ngala J K, Chernova N A, Ma M, Mamak M, Zavalij P Y and Whittingham M S 2004 The synthesis, characterization and electrochemical behavior of the layered $LiNi_{0.4}Mn_{0.4}Co_{0.2}O_2$ compound *J. Mater. Chem.* **14** 214

[63] Nakayama M, Suzuki K, Okamura K, Inoue R, Athouël L, Crosnier O and Brousse T 2010 Doping of cobalt into multilayered manganese oxide for improved pseudocapacitive properties *J. Electrochem. Soc.* **157** A1067

[64] Li C, Han X, Cheng F, Hu Y, Chen C and Chen J 2015 Phase and composition controllable synthesis of cobalt manganese spinel nanoparticles towards efficient oxygen electrocatalysis *Nat. Commun.* **6** 7345

[65] Liu R, Jin D and Yue L 2015 Synthesis and electrochemical properties of Co doped MnO_2 framework with nanofibrous structure *Int. J. Appl. Ceram. Technol.* **12** E59

[66] Kim B C, Justin Raj C, Cho W-J, Lee W-G, Jeong H T and Yu K H 2014 Enhanced electrochemical properties of cobalt doped manganese dioxide nanowires *J. Alloys Compd.* **617** 491

[67] Li H, Wang Z, Chen L and Huang X 2009 Research on advanced materials for Li-ion batteries *Adv. Mater.* **21** 4593